A Thermal Analysis of LASER Beam Welding Using Statistical Approaches

Ariel Flores Monteiro de Oliveira [1], Elisan dos S. Magalhães [1,*], Luiz E. dos S. Paes [2], Milton Pereira [3] and Leonardo R. R. da Silva [2]

[1] Departamento de Energia, Laboratório de Engenharia Térmica Aplicada—LETA, Instituto Tecnológico de Aeronáutica—ITA, São José dos Campos 12228-900, SP, Brazil; arielfmonteiro@gmail.com

[2] Faculdade de Engenharia Mecânica, Centro de Pesquisa e Desenvolvimento em Processos de Soldagem e Manufatura Aditiva—LAPROSOLDA, Universidade Federal de Uberlândia—UFU, Uberlândia 38400-902, MG, Brazil; luiz.paes@ufu.br (L.E.d.S.P.); leorrs@ufu.br (L.R.R.d.S.)

[3] Departamento de Engenharia Mecânica, Universidade Federal de Santa Catarina—UFSC, Florianópolis 88040-900, SC, Brazil; milton.pereira@ufsc.br

* Correspondence: elisan@ita.br

Abstract: Implementing input parameters that match the experimental weld shape is challenging in LASER beam welding (LBW) simulation because the computed heat input and spot for temperature acquisition strongly affect the outcomes. Therefore, this study focuses on investigating the autogenous LBW of AISI 1020 using a three-dimensional heat transfer model that assumes a modified Gaussian heat flux distribution depending on LASER power (Q_w), radius (R), and penetration (h_p). The influence of such variables on the simulated weld bead was assessed through analysis of variance (ANOVA). The ANOVA returns reliable results as long as the data is normally distributed. The input radius exerts the most prominent influence. Taguchi's design defined the studied data reducing about 65% of the simulations compared to a full factorial design. The optimum values to match the computed outcomes to lab-controlled experiments were 2400 W for power (80% efficiency), 0.50 mm for radius, and 1.64 mm for penetration. Moreover, the experimental errors regarding thermocouples positioning were corrected using linear interpolation. A parallel computing algorithm to obtain the temperature field reduces computational costs and may be applied in real-world scenarios to determine parameters that achieve the expected joint quality. The proposed methodology could reduce the required time to optimize a welding process, saving development and experimental costs.

Keywords: LASER welding; heat transfer simulation; parameter optimization; Taguchi's design; parallel computing; Compute Unified Device Architecture (CUDA-C)

1. Introduction

Welding is a critical industrial process among the many joining techniques available [1]. LASER beam welding (LBW) has ample space in the industrial sector. Indeed, the LBW can replace conventional welding techniques because of its many advantages [2]. Besides, LBW presents excellent precision and efficiency characteristics compared to traditional welding methods such as gas tungsten arc welding (GTAW) [3,4] and gas metal arc welding (GMAW) [5]. It permits the welding of complex geometries and dissimilar materials [2], aside from assuring greater levels of product quality [6]. These characteristics apply because this welding technology has high energy density [3,7], high speed [2], high efficiency [6], generating a narrow heat-affected zone (HAZ) [8], and small heat input [9], diminishing residual stresses and thermal distortions [10]. Combining the aspects of the welded joint, including geometrical parameters, such as welding penetration and width, metallurgical microstructure, and mechanical properties, defines if the process has reached the expected welding quality [11]. The practical application of the joint relies on its final characteristics.

Nowadays, controlling the welding process is one of the central industrial problems [12]. The main concern relies on regulating the energy input because it directly affects the quality of the joint. Regarding practical applications, the heat input is defined by different process parameters, such as welding speed, LASER mode and power, and beam diameter [2]. In numerical approaches, the heat input depends on the parameters describing the energy distribution over the sample [13]. For instance, the equation may be dependent on power density, heat flow [14], absorption coefficient, beam radius [15], and total LASER power [16], depending on the heat source model adopted. In this work, the volumetric heat distributed by the LASER over the sample is expressed as a function of LASER power (Q_w), penetration (h_p) radius (R), sample width (L_y), welding velocity (u), and y and z positions along the respective cartesian axes. It consists of a modified Gaussian distribution, proposed by Magalhães et al. [17].

Numerical simulations have been widely studied and applied to welding processes [18–20]. The simulations present other benefits compared to analytical [1] and experimental methods. Although techniques such as high-speed video recording may be applied to study the phenomena occurring during LASER welding, this method is limited to surface examinations [6]. Furthermore, experimental approaches are often costly and time-consuming [21], which leads to an increase in simulations for studying the welding process [1,8]. The computed outcomes can describe the physical phenomena interacting in a vast range of temperatures [12] and study the molten pool dynamics by giving detailed information [22]. As well as in the natural process, the simulated weld is defined by the amount of energy provided by the heat source. Hence, a trustworthy heat transfer model must be used to achieve reliable outcomes. The mathematical model should consider the interactions between LASER and material [23], boundary conditions, and material temperature-dependent properties [24].

The process parameters optimization may be achieved by performing numerical simulations before the actual experiments. In the study conducted by Yu et al. [24], the commercial finite element software Simufact supported the finding of the optimum LASER power (2300 W) and welding speed (3 m/min) that produces the expected final weld bead quality in the LASER welding of a 6061-T6 aluminum alloy. Furthermore, the association between the weld bead geometry and LASER welding process parameters of SUS316L stainless steel was investigated by Ai et al. [25]. The authors could attain the weld shape, including width, reinforcement, and penetration related to welding speed and LASER power variations. These studies corroborate the importance of properly defining the heat input to attain the desired welded joint.

Also, a frequent welding parameter optimization technique is Taguchi's design. This technique allows the optimization of multiple factors to achieve a suitable combination that produces the expected joint quality [26], reducing experimental time and cost by reducing the number of experiments needed [27]. Reddy et al. [28] applied Taguchi's L_{25} orthogonal array to evaluate how the combinations of the parameters such as LASER power, welding speed, beam angle, focal point position, and focal length altered the welding results. Satyanarayana et al. [6] combined CFD simulations and Taguchi's method to determine optimal LBW process parameters that produced a weld bead of 3 mm in depth and minimum fusion diameter.

Another critical process attribute is temperature. Thus, understanding the temperature distributions along the process is crucial to guarantee the desired outputs [5,6], mainly because the quality of the weld bead depends on how the welding processes apply the energy to the joint [9]. The experimental temperature measurement is frequently achieved using thermocouples attached to the sample. The spots of the sensors depend on the target temperature to monitor. Usually, the high energy density of the LASER beam requires the thermocouples to be positioned closer to the bead in LBW than in electric arc welding processes [19]. Indeed, the agreement between the experimental and computed temperatures strongly depends on defining the proper positioning because slight variations can lead to significant temperature deviations. The temperature measurement via thermocouples

may return erroneous values depending on their response time, thermal capacity, and positioning. These effects are extended in regions with very high-temperature gradients, as the conditions are found close to the joint [20].

In other work, Nayak and Roy [22] exposed the challenge of measuring the welding process temperature using thermocouples in locations where the temperature change is fast. The authors developed a temperature correction based on the response lag of type-k thermocouples and validated their responses with commercial CFD codes. Moreover, experimental errors due to thermocouple position may also occur. Magalhães et al. [23] reported that these uncertainties lead to fluctuations in the prediction of thermal properties, such as thermal efficiency.

This study proposes a low-cost methodology to match experimental to simulated data by adjusting the heat input and acquiring the temperature at exact points. For this purpose, this work focuses on obtaining optimum welding simulation parameters. An alternative optimization process is presented to evaluate variations in the power density distribution model and how its parameters, such as radius, penetration, and power, affect the weld bead dimensions computed by the algorithm. A Taguchi design was applied to reduce the number of simulations needed to evaluate the parameter variations. A sensitivity analysis revealed that the input radius is the most sensitive parameter. Indeed, it exerts the most prominent influence on the calculated weld bead. In this case, the optimum values that should be implemented in the algorithm to calibrate the heat input correctly are 2400 W for power, corresponding to 80% efficiency, 0.50 mm for radius, and 1.64 mm for penetration. Moreover, a critical issue that might bias the simulation is the position for temperature acquisition. Experimental placement of the thermocouples presents associated errors. Hence, using the experimentally measured positions in the simulation may return erroneous temperature results. The experimental errors were corrected using linear interpolation to ascertain that the algorithm acquires the temperature at exact spots. After the heat input and position of the sensors were calibrated, the simulated temperatures and weld bead dimensions matched the experimental values. The study was structured as shown in Figure 1.
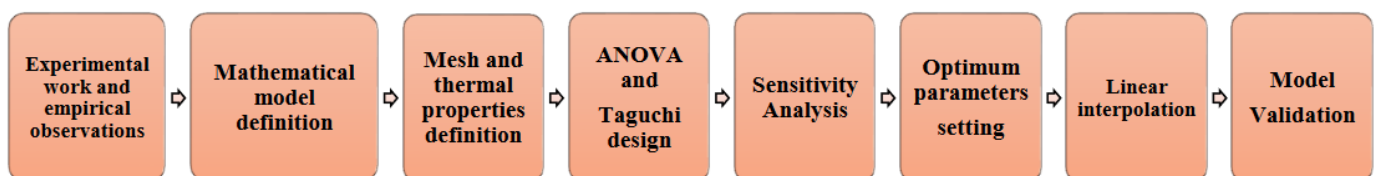

**Figure 1.** Research structure flowchart.

2. Materials and Methods

2.1. Experimental Procedure

The autogenous LBW of the AISI 1020 steel plate of dimension 207 mm × 31 mm × 9.5 mm employed a fiber LASER power source IPG-YLS 10000 with a maximum power output of 3 kW and 0.05 m/s speed. The LASER beam presented Gaussian distribution over the specimen and formed a weld bead size of 45 mm × 1.20 mm × 0.84 mm, as shown in Figure 2. A 15 L/min argon flow was used as a shielding gas to prevent reactions with the atmosphere.

Nine type-k thermocouples were attached along with the weld bead, as shown in Figure 3, to measure the temperature during the process. The red line represents the intended weld bead, and each blue circle represents one sensor, the sensors were named using letters from A to I. A National Instruments USB 6218 board (32 inputs with 16 bits each and 250 Kbps transfer velocity) acquired the thermal data with an acquisition rate of 10 Hz.
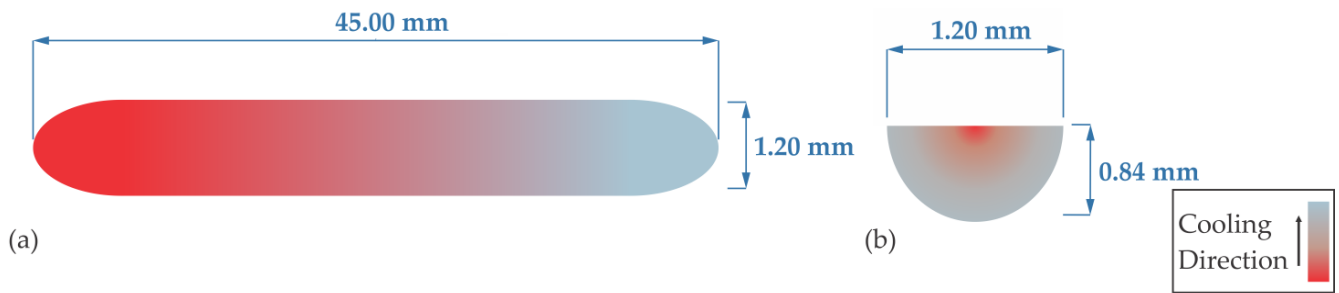
Figure 2. Two-dimensional scheme for experimental weld bead profile: (**a**) Top view. (**b**) Cross-section view.
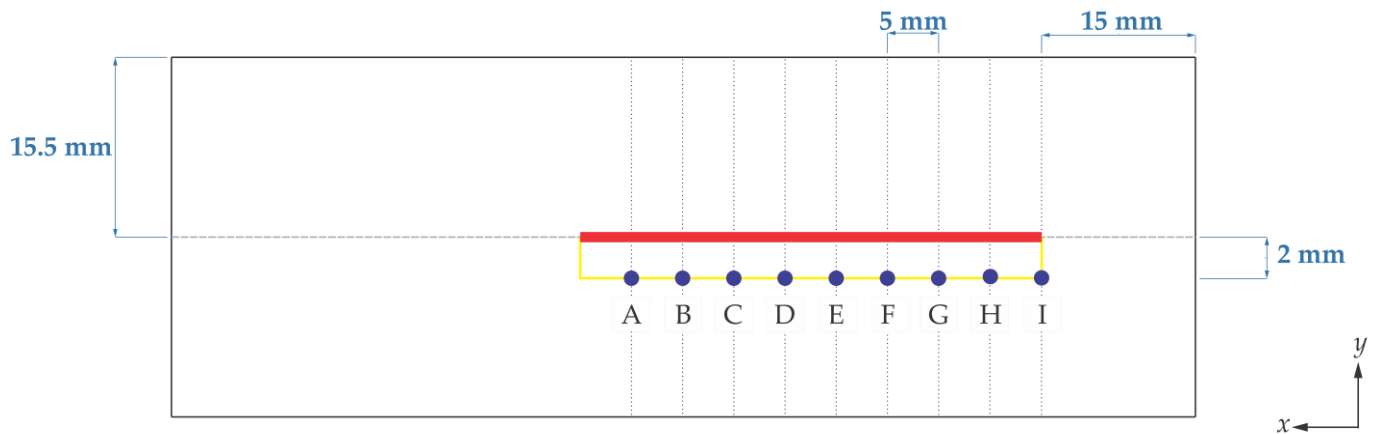
Figure 3. Thermocouples attachment scheme.

2.2. Thermal Model

The thermal model aims to represent the physical conditions in the experimental setup mathematically. Thus, this work models the LASER welding process by discretizing the nonlinear three-dimensional heat diffusion equation [29] expressed in Equation (1) using the finite volume method. The enthalpy function (*H*) models the phase change process.

$$\frac{\partial}{\partial x}\left(\lambda\frac{\partial T}{\partial x}\right) + \frac{\partial}{\partial y}\left(\lambda\frac{\partial T}{\partial y}\right) + \frac{\partial}{\partial z}\left(\lambda\frac{\partial T}{\partial z}\right) + \dot{g} = \frac{\partial H}{\partial t} \tag{1}$$

where *x*, *y*, and *z* are the cartesian coordinates, λ is the nonlinear thermal conductivity, *T* is the numerical temperature, $\dot{g}$ is the generated heat source, and *t* is the time. The enthalpy function (*H*) is described by Equation (2) [30].

$$H = \int_0^T \rho c_p dT + \rho f L \tag{2}$$

where ρ is the specific mass, c_p is the specific heat capacity, *f* is the Heaviside step function, and *L* is the latent heat of fusion.

Boundary conditions of heat loss from the specimen by convection and radiation were considered on all surfaces by the relation expressed in Equation (3), according to Incropera et al. [31].

$$-\lambda\frac{\partial T}{\partial \eta}\bigg|_S = h(T)(T - T_\infty) + \sigma\phi_{rad}(T)(T^4 - T_\infty^4) \tag{3}$$

where η is the normal direction on the surface *S*, *h* is the convection heat transfer function, T_∞ is the initial temperature, σ is the Stefan-Boltzmann constant, and ϕ_{rad} is the emissivity function [32].

Regarding heat distribution, one may apply different mathematical models to represent the heat delivered by the LASER head. This work adopted a conical Gaussian distribution

model proposed by Magalhães et al. [17], which proved suitable for a similar LBW process. The three-dimensional heat source model adopted is expressed in Equation (4).

$$\dot{g} = \frac{Q_w}{0.46025 h_p R^2} \exp\left(-\frac{4.5(z - ut)^2}{R^2}\right) \exp\left(-\frac{4.5\left(z - {L_y}/{2}\right)^2}{R^2}\right)\left(1 - \frac{{x}^1/2}{{h_p}^1/2}\right) \quad (4)$$

where Q_w is the LASER power, R is the welding radius, L_y is the sample width, u is the welding velocity, and z and h_p are parameters for the z-axis, standing for the height distribution over and inside the sample, respectively. h_p is referred to as the welding penetration.

2.3. Numerical Simulation

Slight position variation results in a strong temperature gradient due to the high heat input. Also, the weld pool is small when compared to the whole domain. Ergo, a well-refined mesh must be used. A mesh convergence test defined the minimum number of control volumes in which the domain should be divided to accurately calculate the heat transfer during the process. The temperature was obtained using 400,000, 1,125,000, 2,250,000, 3,200,000, and 7,000,000 control volumes. Only structured meshes were analyzed.

Figure 4 shows the temperature distribution for one temperature sensor for different mesh refinements. It is observed that the mesh with 3,200,000 control volumes shows no significant variation when compared to the domain divided into 7,000,000 control volumes, presenting expressive results. For meshes divided into smaller amounts of control volumes, the deviations concerning the most prominent mesh are substantial and do not express precise temperatures.
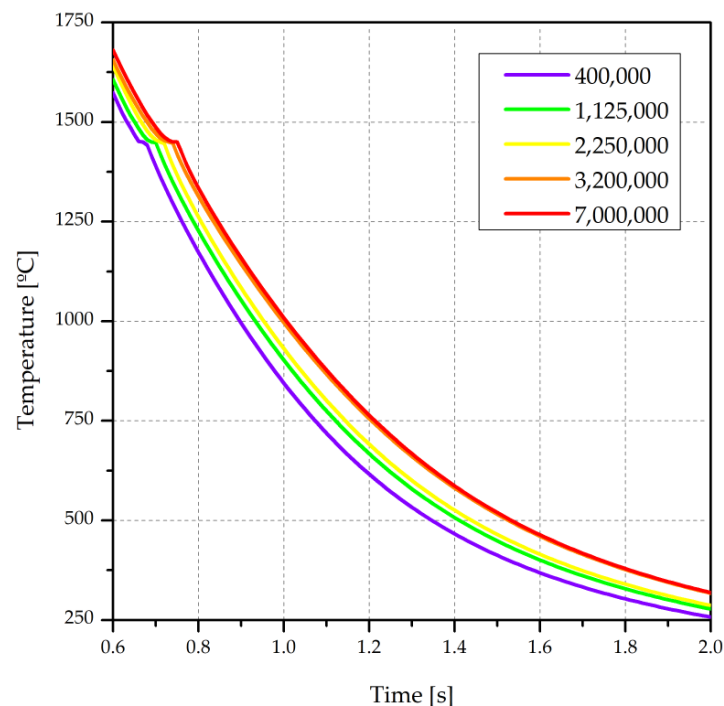
Figure 4. The simulated temperature profile in different mesh conditions.

Therefore, the domain was divided into 3,200,000 volumes, with 400, 200, and 40 nodes along the x, y, and z-axes, respectively. Such structured mesh was selected to correctly represent the heat transfer occurring in the workpiece. Figure 5 shows the cartesian orientation adopted for the three-dimensional domain.
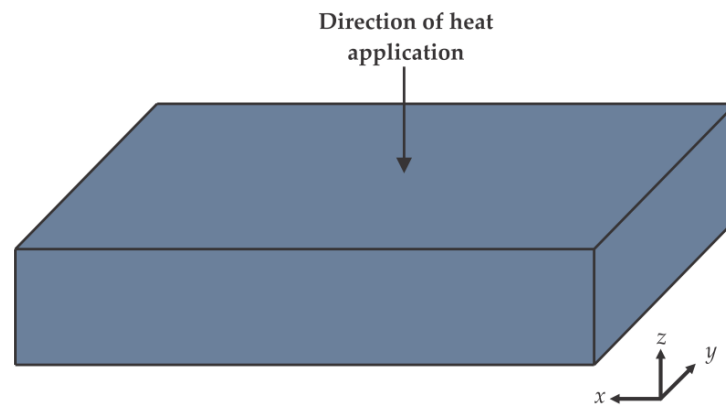
Figure 5. Cartesian orientation of the three-dimensional domain.

Borrmann et al. [33] reported that a high-accuracy thermal model relies on temperature-dependent thermal properties. Therefore, this work considers the thermal properties of AISI 1020 presented in Table 1. These properties are temperature functions and may not cover the entire temperature range involved in the process, and these uncertainties must be considered in the calculated temperatures. The steel melting temperature, or solidus temperature, is considered to be 1450 °C [32].

Table 1. Thermal properties of AISI 1020 as a function of temperature.

Property	Equation		References
Conductivity	$\lambda = 2.50 T^2 \times 10^{-5} - 5.30 T \times 10^{-2} + 57.20$ [W/mK]	(5)	[34]
Volumetric heat Capacity	$\rho c_p = 2.54977 \times 10^6 \times \exp(1.509 T \times 10^{-3})$ [kJ/m³K]	(6)	[32]
Emissivity	$\phi = 8.47 \times 10^{-2} \ln T - 0.3932$	(7)	[35]

2.4. Statistical Analysis

The implemented heat source model considers the power density distribution described in Equation (4). However, to avoid distinctions between the experimental and simulated values for penetration (P_{out}) and radius (R_{out}), it is necessary to calibrate the power density distribution mainly because the sample does not absorb all energy provided by the LASER in the experiments. Thus, implementing experimental parameters for calculating the energy input may return erroneous values. Therefore, this model requires optimal input parameters to properly represent the heat transferred by the LASER to the sample. If the parameters are calibrated enough, the computed weld bead shape should agree with the experimental profile shown in Figure 2.

According to Equation (4), Q_w, R, and h_p would exert the most prominent influence on the response. Such parameters define the first ratio on the right side of the equation, while the other variables used for calculating the heat distribution, such as u, z, L_y, and x, compose the exponents of Equation (4). In addition, z, L_y, and x are applied to calculate other model functions. For instance, L_y also defines the size of each control volume the mesh is divided into; x and z are also used to define how the heat source moves along the sample. Hence, such parameters should not be altered. Furthermore, the work is intended to calibrate the weld bead geometry. The length of the joint is directly acquired by defining the initial and final points of heat application both in the experimental and numerical approaches. Thus, only the radius, or width, and penetration could be calibrated.

In this work, Taguchi's method was applied to determine a factorial design to evaluate if the parameters of the heat source, such as the LASER power (Q_w), radius (R), and penetration (h_p) alter the geometry of the simulated weld bead. The statistical software Minitab® was used as a tool for the design of experiments (DoE). Each of the parameters, LASER beam power (Q_w), radius (R), and penetration (h_p), corresponds to one factor in the software, and three levels are set for each process parameter to perform the numerical simulations.

The experimental data described in Section 2.1 are the baseline for the studied variations. Concerning the radius parameter, the study considered values of 0.40 mm, 0.60 mm, and 0.80 mm. The investigated values for weld bead penetration are 0.42 mm, 0.84 mm, and 1.68 mm, corresponding to 50%, 100%, and 200% of the experimental value of the weld bead.

Regarding LASER power, the process efficiency must be accounted for because the heat provided by the LASER is not transferred exclusively to the sample and depends on weld bead dimensions, heat source, and material properties. Tadamalle et al. [36] calorimetrically measured the LASER output, resulting in an energy transfer efficiency of 87%. Nevertheless, Fakir et al. [37] found that 76% of the emitted energy is transferred to the sample, considering convective and radiation heat losses. Silva et al. [38] obtained an average of 79.5% LBW absorption efficiency in the AISI 1020 steel. This literature served as guidelines for choosing the considered values: 2.7 kW, 2.4 kW, and 2.1 kW, corresponding to LASER efficiencies of 90, 80, and 70%, respectively. Table 2 summarizes the levels of each factor.

Table 2. Statistical analyses factors and levels.

Factor	Levels		
	1	2	3
Power (kW)	2.10	2.40	2.70
Radius (mm)	0.40	0.60	0.80
Penetration (mm)	0.42	0.84	1.68

The computation of the weld bead sizes for all level combinations would require 27 algorithm runs. However, only nine runs are necessary to perform the analysis using Taguchi's design, consisting of a $^1/_3$ fractional design. Table 3 shows the design of the experiments, besides the values calculated by the algorithm for the weld bead radius (R_{out}) and penetration (P_{out}). When applying the correspondent levels association, the numerical responses correspond to the weld bead size predicted by the code. After the computation, the measurements were obtained using the software Paraview.

Table 3. Taguchi's design of experiments adopted.

Pre-Test	Levels			Responses	
	Q_w	R	h_p	R_{out} (mm)	P_{out} (mm)
1	3	1	1	1.09	0.99
2	3	2	2	0.96	0.94
3	3	3	3	0.37	0.52
4	2	1	2	1.07	1.07
5	2	2	3	0.54	0.71
6	2	3	1	0.58	0.48
7	1	1	3	0.62	0.90
8	1	2	1	0.62	0.49
9	1	3	2	0.54	0.47

Furthermore, an analysis of variance (ANOVA) was performed to quantify the influence of the factors on the response and evaluate possible interactions between factors. The ANOVA tables include the number of degrees of freedom (*DF*), sum of squares (*SS*), mean square (*MS*), Fisher test statistic (*F*), and *p*-value based on the *F*-value. This analysis provides the significance of the process parameters on the output response. One may check if the ANOVA results are valid by examining data residuals. For instance, the residuals must be normally distributed and independent, presenting no correlation [39].

Besides, a sensitivity analysis was performed to corroborate that the model correctly represents the physical phenomena involved in LBW. As well as the analysis performed using Taguchi's design, this test allows the investigation of the influence of Equation (4) input parameters Q_w, R, and h_p on the computed radius and penetration (R_{out} and P_{out}). However,

different level combinations are accounted for. In this case, the focus is individually evaluating the influence of the factors. Hence, the levels vary only for one parameter. At the same time, the other two are constants. The values used for this investigation are the same as shown in Table 2. These analyses supported the finding of the optimal input parameters. Indeed, the algorithm parameters are not necessarily equal to the experimental configuration set.

3. Statistical Evaluation of the Heat Source Input Parameters

The analyses of the simulations determined by Taguchi's design are illustrated in Figures 6–8. The graphs expose how each parameter of the calculated heat distribution, respectively LASER beam power (Q_w), radius (R), and penetration (h_p), alter the forecasted geometry of the weld bead, considering the averages of the output data. Such information is necessary to support finding the optimal combination of energy distribution parameters, i.e., the energy input value that creates the intended weld bead, defined by the experimental observation shown in Figure 2.
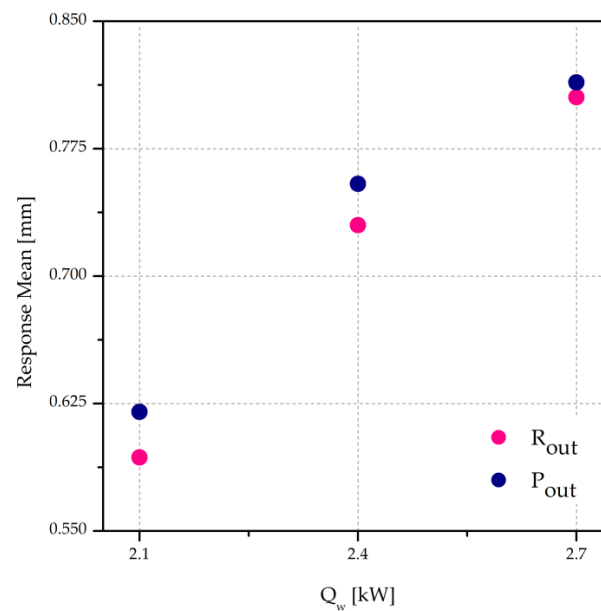

Figure 6. Variations of R_{out} and P_{out} due to different LASER powers (Q_w) applied.
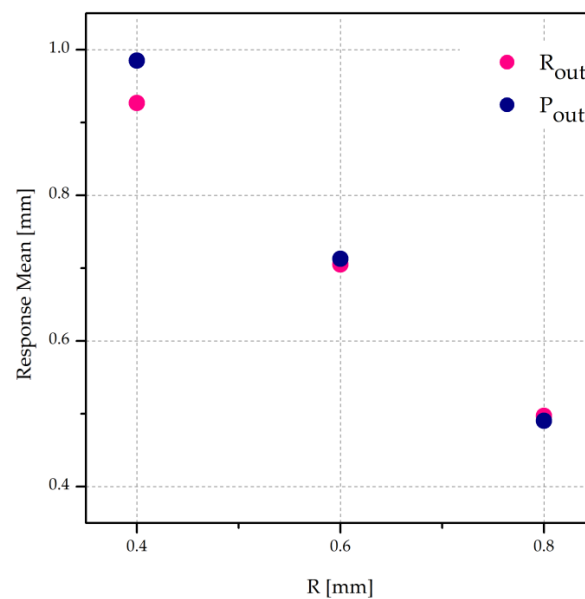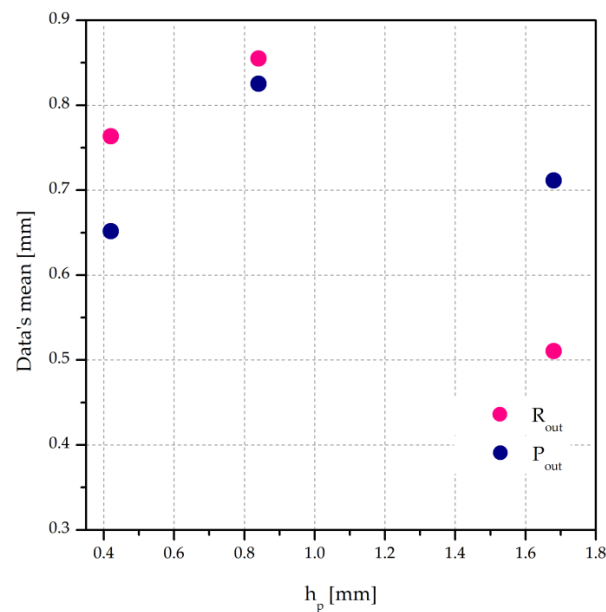

Figure 7. Variations of R_{out} and P_{out} due to different radii (R) applied.

Figure 8. Variations of R_{out} and P_{out} due to different penetrations (h_p) applied.

Figure 6 shows the variations caused in the computed geometry when the three levels of Q_w (2.1 kW, 2.4 kW, and 2.7 kW) are considered. The variables are proportional. In addition, the line slopes for the responses are similar. It means that enhancing the power enlarges and deepens the joint. The increase in the weld pool size at greater Q_w conditions may be justified once a more significant energy input is associated with a rise in LASER power. Observing Equation (4), one may infer that Q_w is proportional to the heat input. Thus, more energy would be available to cause a phase change in the material. This way, more energy would be directed to the surface of the sample. The algorithm reflects this effect.

In addition, Figure 7 exposes the effects of R on the computed responses. The parameter is inversely proportional to the calculated dimensions. Also, the behaviors of the responses are comparable. It is essential to notice that this demeanor is found due to how the heat input calculation is performed. According to Equation (4), R is accounted for as a squared denominator. Therefore, considering a greater width in the heat distribution model induces a lower process energy density, resulting in a narrower and shallower calculated weld bead.

The influence of h_p variations is similar for R_{out} and P_{out}. By observing the locations of the points on the graph displayed in Figure 8, it is possible to notice that h_p increases both magnitudes for penetrations between 0.42 mm and 0.84 mm and decreases the computed sizes from 0.84 mm to 1.68 mm. Thus, there is a maximum value for which the h_p may increase the energy amount supplied to the sample. The difference between the heating and cooling rates may cause the maximum answers. Suppose the heat is removed from the molten pool at the same rate as the LASER beam supplied to the sample. The available energy would be constant, so no further melting or penetration can occur. The phase change may be assumed as a quasi-steady state in this condition.

Based on the simulations performed according to Taguchi's design, one may infer which factor influences the weld bead dimensions more significantly by calculating the delta. It is given by the difference between the highest and lowest average response values of the factors. Hence, the more significant the delta, the greater the factor effect on the output value. The answer for the R_{out} means, and the delta values for each element are exhibited in Table 4. R has the most prominent influence, followed by h_p and Q_w.

Table 4. Evaluation of input parameters significance over the radii responses (R_{out}) according to the delta.

Factor	Levels			Delta	Effects Rank
	1	2	3		
Power (Q_w)	0.5933	0.7300	0.8053	0.2120	3
Radius (R)	0.9267	0.7050	0.4970	0.4297	1
Penetration (h_p)	0.7633	0.8850	0.5103	0.3441	2

Analog to R_{out}, R exerts the most considerable influence on P_{out}. However, h_p and Q_w effects are comparable. The delta values for this response are expressed in Table 5.

Table 5. Evaluation of input parameters' significance over the penetration responses (P_{out}) according to the delta.

Factor	Levels			Delta	Effects Rank
	1	2	3		
Power (Q_w)	0.6200	0.7543	0.8140	0.1940	2
Radius (R)	0.9850	0.7130	0.4903	0.4947	1
Penetration (h_p)	0.6517	0.8253	0.7113	0.1737	3

An analysis of variance was performed to confirm that the effects of the parameters are statistically significant. The significance level α was set at 5%. The null hypothesis for the *p*-value states no association between the term and the response. If the *p*-value is less than 0.05, the null hypothesis must be rejected, and one should consider the influence of the factor on the answer.

Table 6 shows the ANOVA for R_{out}. The *p*-value for all the factors is below 0.05; thus, all the parameters are statistically significant. The calculus of the degrees of freedom (DF), the sum of squares (SS), mean squares (MS), F, and *p*-values can be found in Devore [40]. Moreover, one may employ the F value to quantify how a factor explains the deviations in the response. In this way, the effects rank is analogous to that inferred by deltas' calculation, being R is the most influential parameter followed by h_p and Q_w. The error values are missing because the results are obtained through simulations, so replications are unnecessary.

Table 6. Investigation of statistical significance of Q_w, R, and h_p, on R_{out} through ANOVA.

| Factor	DF	SS	MS	F	*p*-Value
Power (Q_w)	2	0.069297	0.034648	29.78	0.032
Radius (R)	2	0.277014	0.138507	119.05	0.008
Penetration (h_p)	2	0.191207	0.095603	82.17	0.012
Residual	2	0.002327	0.001163		
Error	--	--	--		
Total	8	0.539844			

Regarding P_{out}, only the influence of R is statistically significant, as the *p*-values for Q_w and h_p are over 0.05, as shown in Table 7. It means that variations of Q_w and h_p should not explain the variations in the simulated penetration. The F values express the same tendency shown in Table 5, as R has the most prominent influence while Q_w and h_p show equivalent behaviors.

However, the effects of varying Q_w and h_p seem relevant on P_{out}, as indicated in Figures 6 and 8. Thus, the residuals should be analyzed. First, a normal probability plot was obtained using Minitab to check if the data were normally distributed. Indeed, the ANOVA results may lead to misunderstandings regarding P_{out} once the residuals are non-normally distributed, as shown in Figure 9. The fitted normal distribution line is represented in red. The

plot should resemble a straight line if the error distribution is normal. However, the points seem aligned three by three at residuals of circa -0.03, 0, and 0.05, revealing the non-normality of data. Hence, the p-values expressed in Table 7 can be inaccurate.

Table 7. Investigation of statistical significance of Q_w, R, and h_p, on P_{out} through ANOVA.

| Factor	DF	SS	MS	F	*p*-Value
Power (Q_w)	2	0.059242	0.029621	6.30	0.137
Radius (R)	2	0.368260	0.184130	39.13	0.025
Penetration (h_p)	2	0.046716	0.023358	4.96	0.168
Residual	2	0.009411	0.004705		
Error	--	--	--		
Total	8	0.483628			
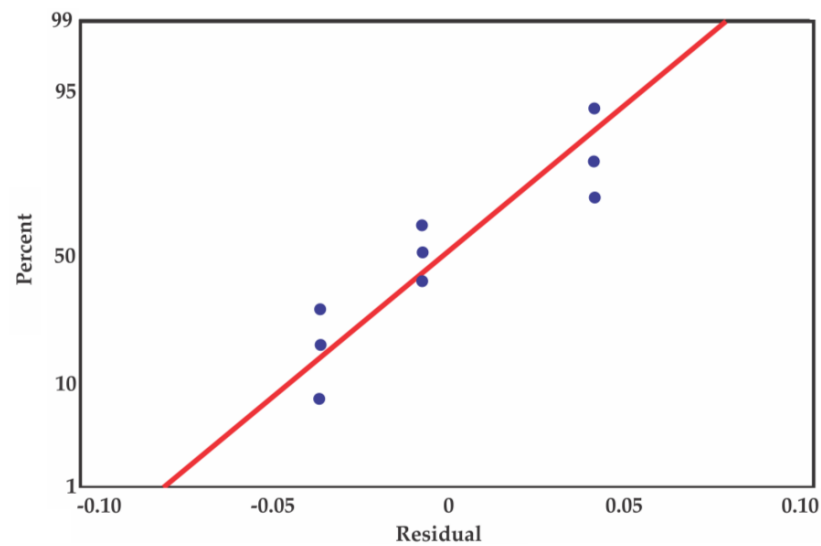
Figure 9. Distribution of values for P_{out} residuals related to the normal probability.

Further evidence that ANOVA may return erroneous results is the trend shown in Figure 10. The residuals should be randomly distributed, but a certain tendency is observed.
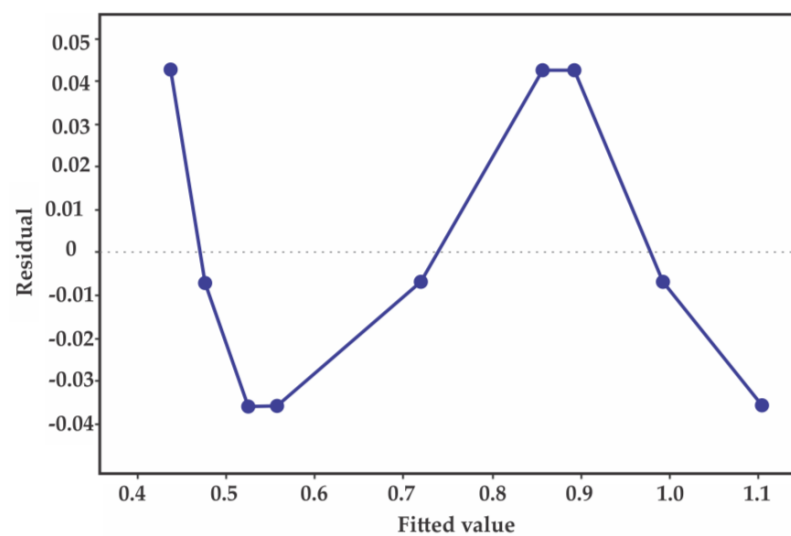
Figure 10. Non-random distribution of residuals for P_{out} mean.

A sensitivity analysis corroborated the ANOVA results and verified if Taguchi's fractional design suits the intended investigation. Firstly, variations in the calculated measures R_{out} and P_{out} due to R are investigated. Figure 11 expresses this influence. Each curve corresponds to the computed weld pool deviations under two different power conditions, 2.7 kW and 2.4 kW. As R in Equation (4) is always a squared denominator, accounting for bigger radii values results in less energy provided to the sample. Consequently, a smaller weld pool size is obtained. This tendency confirms the behavior found when investigating Taguchi's design through ANOVA.
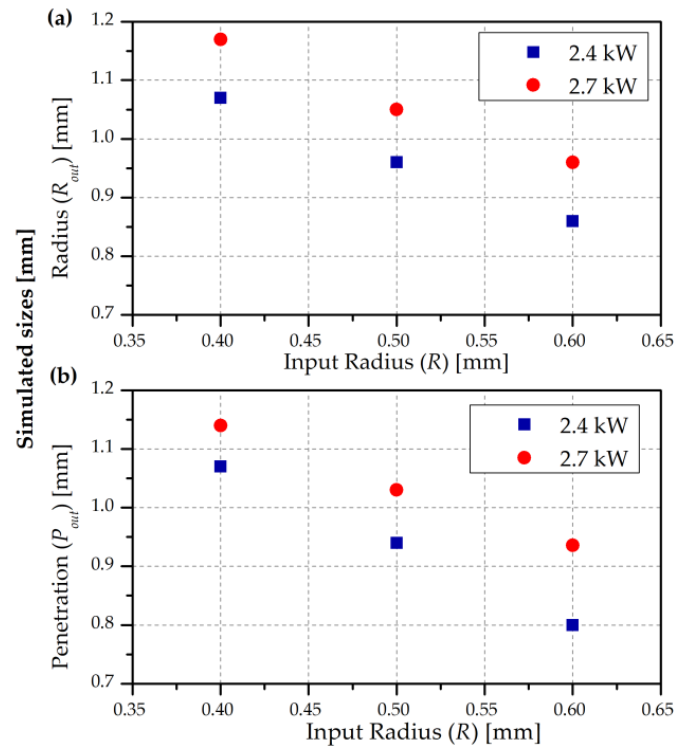
Figure 11. Input radius variation effects in computed weld bead sizes, with h_p fixed at 0.84 mm: (**a**) variation effects over computed radii; (**b**) variation effects over computed penetration.

Table 8 shows the answers for the different radii and calculated delta under each power condition. In this case, the calculations consider the absolute response values. There is no delta variation for the different power conditions. Hence, the factor influence on R_{out} is analogous and independent of the implemented Q_w.

Table 8. Evaluation of delta due to input radius effects on R_{out} under different power conditions.

Q_w (kW)	R (mm)	R_{out} (mm)	Delta
	0.40	1.17	
2.7	0.50	1.05	0.21
	0.60	0.96	
	0.40	1.07	
2.4	0.50	0.96	0.21
	0.60	0.86	

Table 9 expresses the simulated penetration and delta values for each power set. Besides the slight deviation in R influence over P_{out} under the analyzed power conditions, the values are comparable.

Table 9. Evaluation of delta due to input radius effects on P_{out} under different power conditions.

Q_w (kW)	R (mm)	P_{out} (mm)	Delta
	0.40	1.14	
2.7	0.50	1.03	0.20
	0.60	0.94	
	0.40	1.07	
2.4	0.50	0.94	0.27
	0.60	0.80	

Figure 12 exhibits how variations in the penetrations accounted for in Equation (4) influence the simulated weld bead geometry. This factor presents different effects depending on its magnitude. From 0.42 mm to 0.84 mm, an increase in input penetration results in greater computed radii. The inverse is observed from 0.84 mm to 1.68 mm. Similar to Taguchi's analysis, implementing h_p values around 0.84 mm generates the maximum weld bead penetration for this case. Both statistical analyses have analogous explanations. In opposition, increasing h_p produces a deeper weld bead, enlarging the simulated penetration for all power states, besides being inversely proportional to the energy input. Considering R and Q_w fixed factors, one may notice that changes in h_p do alter the simulated geometry, revoking ANOVA results for this factor.
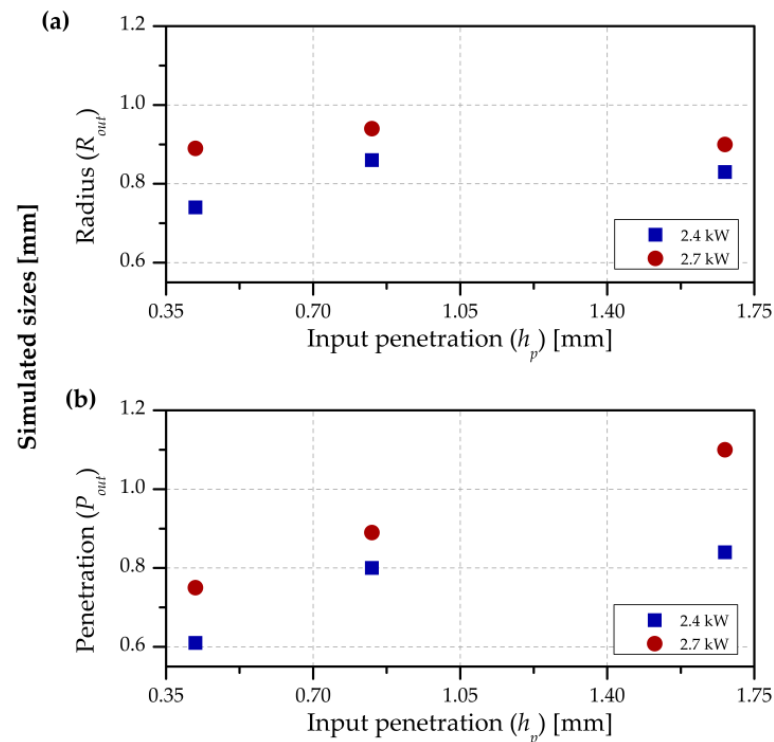

Figure 12. Input penetration variation effects in computed welding radius, with R fixed at 0.6 mm: (**a**) variation effects over computed radii; (**b**) variation effects over computed penetration.

Table 10 expresses delta values for penetration variance under 2.4 kW and 2.7 kW. This factor has a similar influence over R_{out} for all the power conditions, as shown in Figure 12.

Subjecting the sample to 2.7 kW or 2.4 kW does not cause a relevant difference in the influence caused by the accounted penetration on P_{out}, as shown in Table 11.

Fixing the input values for radius and penetration at 0.60 mm and 0.84 mm, respectively, allowed the examination of the effects of LASER power variation. The constant

input values correspond to the experimental weld bead measures. As the LASER power increases, so do the numerical answers, as demonstrated in Figure 13. An increase in power results in more heat transfer to the sample, resulting in a greater affected area. Thus, more material is subjected to melting, enlarging, and deepening of the joint.

Table 10. Evaluation of delta due to input penetration effects on R_{out} under different power conditions.

Q_w (kW)	h_p (mm)	R_{out} (mm)	Delta
	0.42	0.89	
2.7	0.84	0.94	0.05
	1.68	0.90	
	0.42	0.74	
2.4	0.84	0.86	0.09
	1.68	0.83	

Table 11. Evaluation of delta due to input penetration effects on P_{out} under different power conditions.

Q_w (kW)	h_p (mm)	R_{out} (mm)	Delta
	0.42	0.75	
2.7	0.84	0.89	0.35
	1.68	1.10	
	0.42	0.61	
2.4	0.84	0.80	0.23
	1.68	0.84	
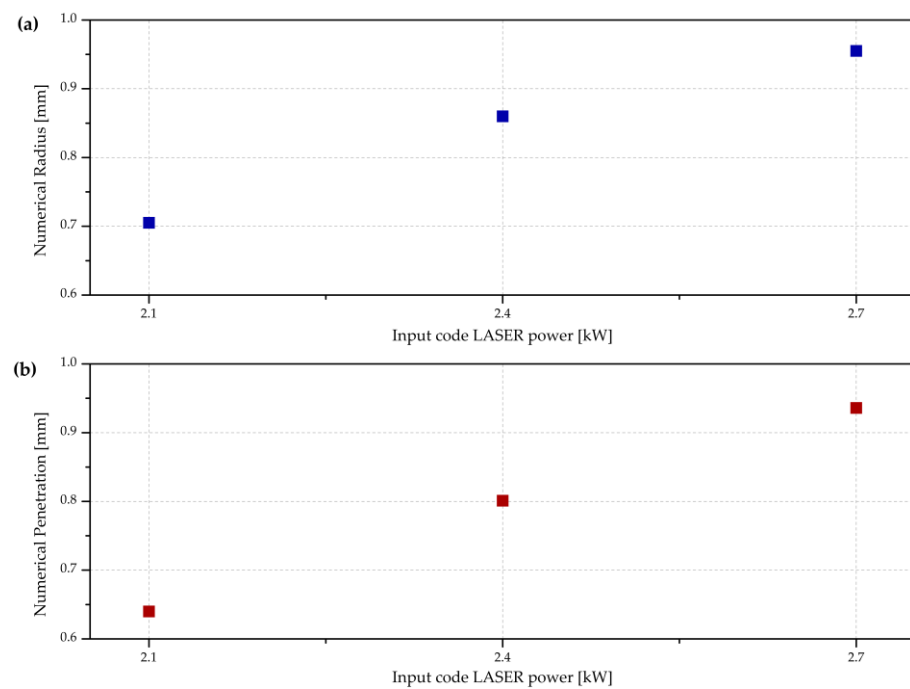
Figure 13. Input power variation effects in computed welding pool size, with R and h_p fixed at 0.6 and 0.84, respectively: (**a**) variation effects over computed radii; (**b**) variation effects over computed penetration.

Beyond, LASER power is directly proportional to computed radius and penetration. It also presents a similar level of influence on the response since delta values are comparable, as shown in Table 12, so increasing the LASER power results in more energy provided to the sample, which is distributed to cause a similar phase change along the weld pool diameter and penetration.

Table 12. Evaluation of delta due to input power effects on R_{out} and P_{out}.

| Q_w (kW)	2.4	2.7	Delta
R_{out} (mm)	0.86	0.96	0.25
P_{out} (mm)	0.80	0.94	0.30

The sensitivity analysis delta values reveal no relevant interactions between R and Q_w, nor h_p and Q_w, since the impact of varying such parameters is comparable under different power conditions. Similar tendencies are observed by comparing the sensitivity analysis results and outcomes obtained using Taguchi's design. Both methods indicate that the weld bead sizes (R_{out} and P_{out}) decrease by applying larger radii values in the heat input calculation. Indeed, Equation (4) shows that R is inversely proportional to the generated heat source. Thus, reducing the heat provided by the LASER to the sample would result in a narrower and shallower weld bead. In opposition, increasing process efficiency also increases the amount of energy supplied to the sample, so deeper and larger weld beads should be simulated. Taguchi and sensitivity analyses confirm this behavior.

Regarding the effects of input penetration in the generated heat, the behavior is equivalent in both examinations for R_{out}. However, a discrepancy is found when observing P_{out} deviations. As seen, variances in any parameter implemented in the equation imply changes in the response. As ANOVA results lead to inferring some factors are not statistically significant, but indeed they are, one should consider the outcomes of the sensitivity analysis. Besides, the influence level is different for each factor.

The considerations obtained through the statistical analysis assist in the parameter combination selection. To this extent, different combinations must be regarded, considering the effects of each parameter evaluated on the response, to obtain the expected output.

4. Thermal Gradient Significance

Investigating the temperature variation along the *y*-axis assessed the significance of the thermal gradient involved in the LASER welding process. Suppose the LASER is focused at 15.5 mm, the workpiece centerline. The temperature was evaluated at three different points, as shown in Figure 14. The first point is 2.5 mm away from the centerline. From this point, 1 mm deviation is added to define the positions of the second and third points.
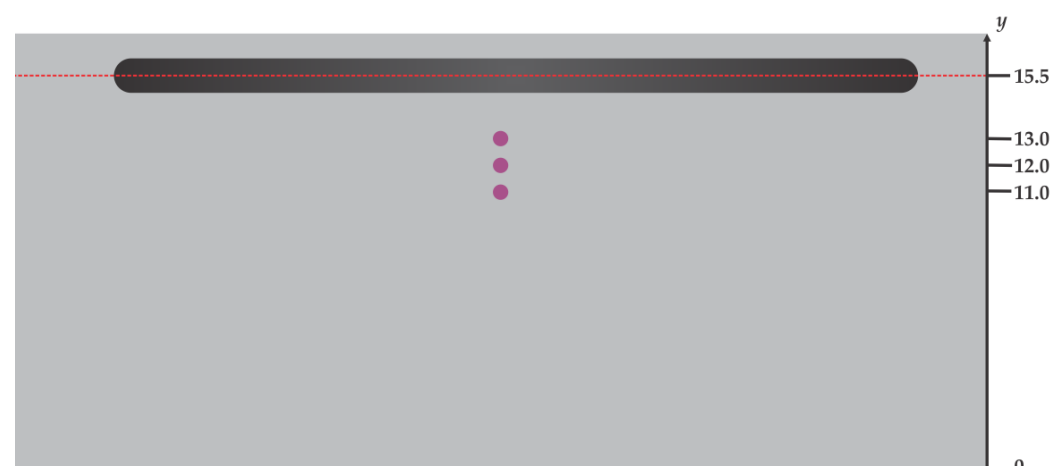
Figure 14. Positions for thermal gradient analysis.

Figure 15 expresses the peak temperatures acquired in the three locations. At 11 mm, the peak temperature attained is 168.14 °C. This value increases 188.33 °C at 12 mm, assuming 356.47 °C at this position. Moving forward another millimeter, the peak temperature obtained is 600.46 °C, about 244 °C greater at 13 mm compared to its previous point. The significance of the temperature variation corroborates the high thermal gradient, even with slight position deviations.
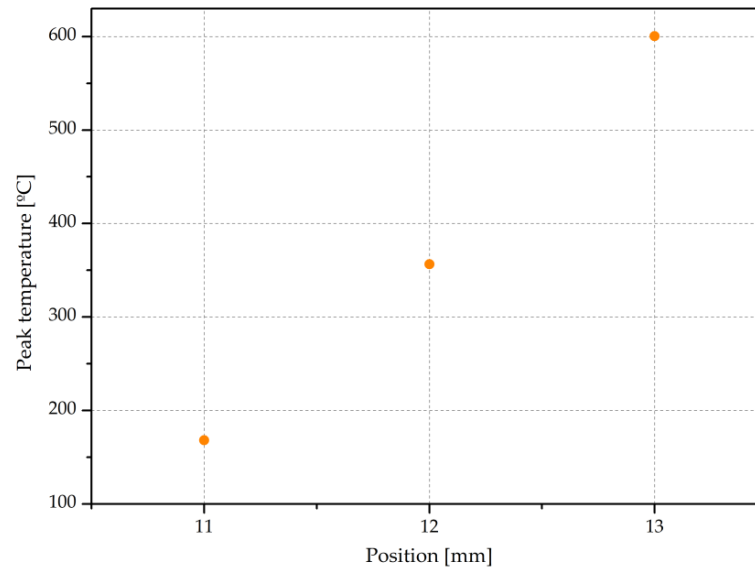

Figure 15. Temperature variation along the y-axis.

5. Definition of the Numerical Parameters

5.1. Sensor Positioning

The planned thermocouple arrangement is shown in Figure 3. The weld bead is at the workpiece centerline, at 15.5 mm from the y-axis origin, i.e., the border of the sample, and the thermocouples are placed with a 2.0 mm deviation from the weld bead. As the temperature distribution is symmetric, temperatures in positions 17.5 mm and 13.5 mm must be the same since they present the same distance from the workpiece centerline.

The sensors were manually attached to the sample. Therefore, there were deviations from the thermocouples' actual and planned positions. Table 13 expresses the exact thermocouple positions experimentally measured along the y-axis, representing the distance between the thermocouple and sample border, and the spacing between the heat source and the sensor. Furthermore, it is considered that the observed positions match the ideal along the x-axis.

Table 13. Real thermocouples positions.

| Sensor	y-Axis Position (mm)	Deviation from the Joint (mm)
A	13.28 ± 0.78	2.22
B	13.59 ± 0.78	1.91
C	12.97 ± 0.77	2.53
D	13.11 ± 0.77	2.39
E	12.76 ± 0.77	2.74
F	13.18 ± 0.77	2.32
G	12.90 ± 0.77	2.60
H	12.97 ± 0.77	2.53
I	12.99 ± 0.77	2.51

The implemented thermocouples' spots must be accurate since the code evaluates the temperature at valid points. According to the high thermal gradient exposed in Section 4, the experimental positions displayed in Table 13 must be considered rather than planned, despite slight errors. Moreover, adjusting the experimental data before implementation is necessary.

The numerical positions correctly reflecting the experimental thermal cycle were obtained by linear interpolation, considering the peak temperatures acquired during the welding cycle and places where the sensors reached these temperatures. Table 14 expresses the experimental and numerical peak temperatures and positions along the *y*-axis where they were acquired. The required adjustments are minor for every position. If the temperature is evaluated at adequate spots, the numerical sensors could attain temperatures close to those in the experiments with no significant deviations. Regarding the peak temperatures, the negative error percentage values are found when the simulated temperature exceeds the experimental temperature.

Table 14. Experimental and numerical thermocouples position along the *y*-axis and peak temperatures.

| Sensor	Position *y*-Axis (mm)		Error Percentage (%)	Peak Temperature (°C)		Error Percentage (%)
	Experimental	Numerical		Experimental	Numerical	
A	13.28 ± 0.78	14.00 ± 0.79	−5.42	321.37 ± 3.72	321.21 ± 3.72	0.05
B	13.59 ± 0.78	12.07 ± 0.75	11.18	359.94 ± 4.10	359.79 ± 4.10	0.04
C	12.97 ± 0.77	12.00 ± 0.75	7.48	239.47 ± 2.90	238.41 ± 2.89	0.44
D	13.11 ± 0.77	13.00 ± 0.77	0.84	275.34 ± 3.26	274.85 ± 3.25	0.18
E	12.76 ± 0.77	13.50 ± 0.78	−5.80	290.46 ± 3.41	309.21 ± 3.60	−6.45
F	13.18 ± 0.77	12.99 ± 0.77	1.44	266.50 ± 3.17	255.89 ± 3.06	3.98
G	12.90 ± 0.77	12.50 ± 0.76	3.10	246.70 ± 2.97	246.25 ± 2.97	0.18
H	12.97 ± 0.77	13.00 ± 0.77	−0.23	273.54 ± 3.24	274.85 ± 3.25	-0.48
I	12.99 ± 0.77	11.24 ± 0.73	13.47	191.14 ± 2.42	189.35 ± 2.40	0.94

Figure 16 presents the final positioning of the thermocouples concerning the weld bead for the experimental and numerical analyses and their respective error percentage bars. Besides the error percentage values in Table 14, the numerical positions assume values within the applicable error rates associated with possible measurement errors for all the sensors. The sensors were named from letters A to I to match the positions shown in Figure 3.
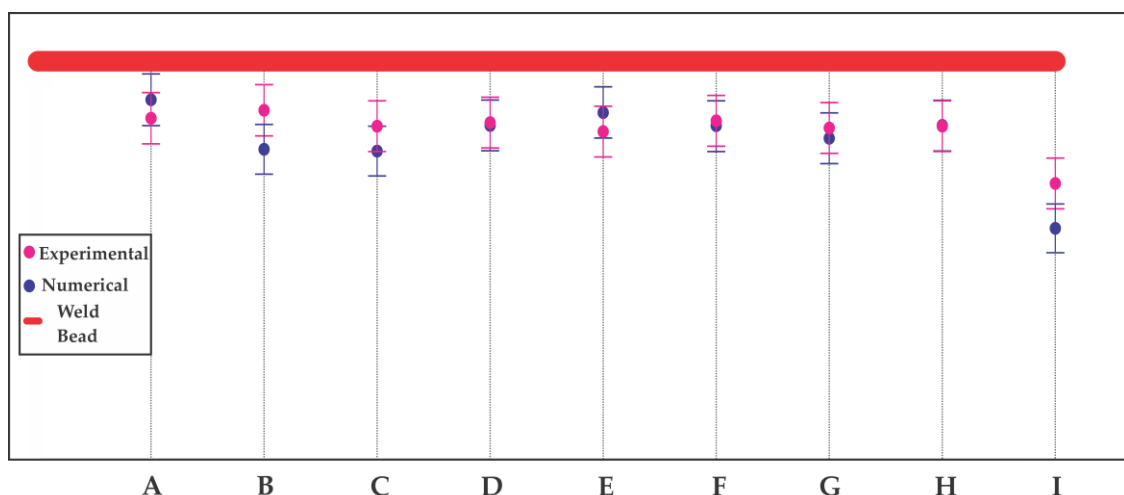

Figure 16. Thermocouples positioning.

5.2. Heat Source Model Parameters

The implementation of the experimental sizes on the algorithm for calculating the heat input through Equation (4) led to the weld bead profile shown in Figure 17. The presented geometry does not match the experimental weld bead. The weld bead sizes compared to the experimental are 0.9 mm and 0.17 mm greater for width and penetration, respectively. Hence, the parameters should be calibrated to decrease both sizes.
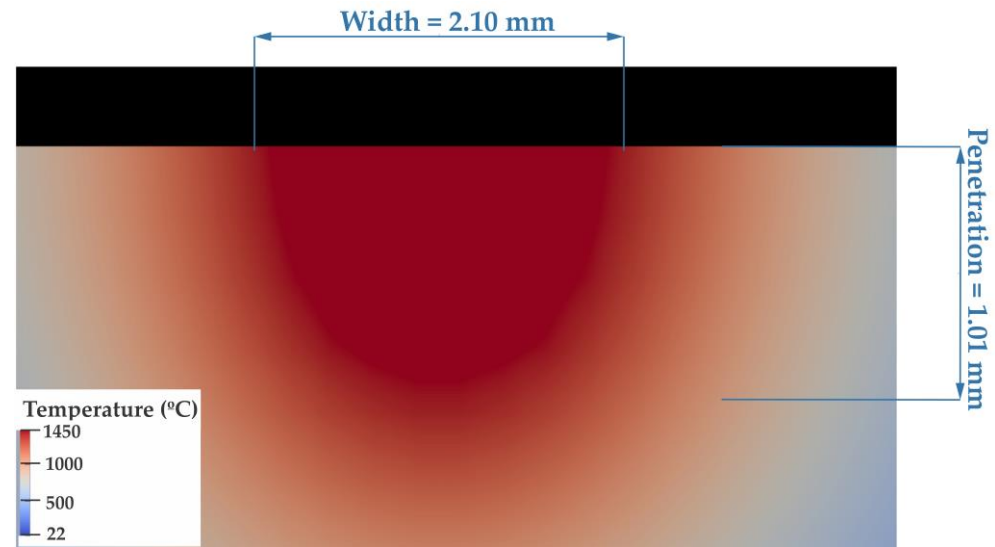
Figure 17. Cross-section view of the simulated weld bead considering experimental data (R = 0.6 mm, h_p = 0.84 mm, and Q_w = 3 kW).

The results in Section 3 were used to support the balance of R, h_p, and Q_w values to correctly calculate the heat input. The considered efficiency of the LASER is 80% of the actual power applied to the sample. The radius is 0.1 mm lesser than that experimentally measured. Besides, the penetration corresponds to double that of the experimental. Implementing these parameters in the energy density distribution model could precisely represent the heat transferred to the sample. Figure 18 presents a cross-section micrograph of the experimental weld bead and numerically obtained weld bead profile. The dimensions of the ciphered numerical weld bead are 0.605 mm for welding radius and 0.843 mm for penetration, so the numerical to experimental sizes' deviations are 5 μm regarding weld bead radius and 1 μm regarding penetration.
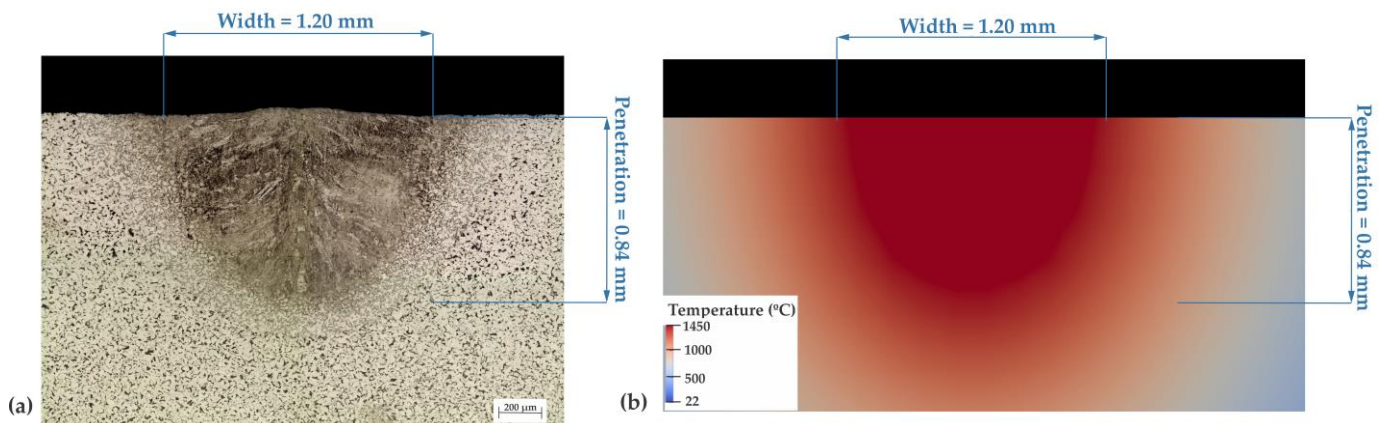
Figure 18. Weld bead profiles: (**a**) cross-section micrograph of the experimental weld bead, exposing fused zone (FZ), heat-affected zone (HAZ), and base metal (BM); (**b**) cross-section of the numerical weld bead, colored by temperature.

The similarity between the weld beads profiles shown in Figure 18 is further corroboration of implementing the proper input parameters in the model once the code acquired outputs comparable to the experimental process results.

This way, one may infer that the adjusted input parameters are accurate and reflect the real heat input and thermal cycle suffered by the AISI 1020 specimen during autogenous LASER welding. A summary of the implemented parameters is shown in Table 15.

Table 15. Numerical input parameters for autogenous AISI 1020 LASER welding.

Input Parameter	
Power	2400 W
Weld bead radius	0.50 mm
Weld bead penetration	1.64 mm
Thermal properties	See Table 1.
Thermocouples positioning	See Table 14.

6. Conclusions

This paper proposed a methodology based on statistical and mathematical evaluations to calibrate LBW simulation parameters to match numerical to experimental data. Besides the weld shape, the propounded procedure could also compare the temperature acquired at nine locations. The main results may be summarized as follows:

i. The calculated weld bead does not match the experimental geometry if the observed sizes are implemented for calculating the power density distribution function through the heat source model adopted (Equation (4)). Hence, the parameters should be calibrated to account for the correct heat distribution over the sample.

ii. In order to obtain the optimal combination of the heat input parameters, the influences of LASER power (Q_w), radius (R), and penetration (h_p) over the simulated weld bead were assessed.

iii. Using a factorial design defined by Taguchi's method reduced 65% of the simulations performed, decreasing computational costs.

iv. ANOVA may be applied to assess the statistical significance of parameter variation over the simulation responses and quantify the most prominent influence if the data is normally distributed. In this case, ANOVA returned reliable results for investigating the effects of R and Q_w deviations but did not suit h_p evaluation. The results were corroborated through a sensitivity analysis.

v. Besides computing the exact heat input, a critical issue that might bias the simulation is the position for temperature acquisition. In LBW of AISI 1020, the sample thermal properties and high energy provided by the LASER create an expressive temperature gradient if the measures are acquired at different spots with micrometer deviations.

vi. The experimental placement of the thermocouples presents associated errors. Hence, simulating temperatures at such spots may return erroneous results. The proper position for each of the nine sensors was selected by linear interpolation.

The adopted methodology may be used to obtain optimum input parameters for LBW simulations. With faster CFD analysis, achieving the expected joint quality is possible. Thus, the procedure could reduce the required time to optimize a welding process, saving on development costs.

Author Contributions: Conceptualization, A.F.M.d.O. and E.d.S.M.; methodology, A.F.M.d.O. and E.d.S.M.; software, E.d.S.M.; validation, A.F.M.d.O.; writing—original draft preparation, A.F.M.d.O.; writing—review and editing, A.F.M.d.O., E.d.S.M., L.E.d.S.P., L.R.R.d.S. and M.P.; supervision, E.d.S.M. and L.E.d.S.P.; experiments, L.E.d.S.P. and M.P. All authors have read and agreed to the published version of the manuscript.

Conflicts of Interest: The authors declare no conflict of interest.

References

1. Casalino, G.; Contuzzi, N.; Minutolo, F.M.C.; Mortello, M. Finite Element Model for Laser Welding of Titanium. *Procedia CIRP* **2015**, *33*, 434–439. [CrossRef]
2. Kubiak, M.; Piekarska, W. Comprehensive Model of Thermal Phenomena and Phase Transformations in Laser Welding Process. *Comput. Struct.* **2016**, *172*, 29–39. [CrossRef]
3. Kik, T. Heat Source Models in Numerical Simulations of Laser Welding. *Materials* **2020**, *13*, 2653. [CrossRef] [PubMed]
4. Gonçalves e Silva, R.H.; dos Santos Paes, L.E.; de Sousa, G.L.; Marques, C.; Viviani, A.B.; Schwedersky, M.B.; da Costa Pinto, T.L.F. Design of a Wire Measurement System for Dynamic Feeding TIG Welding Using Instantaneous Angular Speed. *Int. J. Adv. Manuf. Technol.* **2019**, *101*, 1651–1660. [CrossRef]
5. Truppel, G.H.; Angerhausen, M.; Pipinikas, A.; Reisgen, U.; dos Santos Paes, L.E. Stability Analysis of the Cold Metal Transfer (CMT) Brazing Process for Galvanized Steel Plates with ZnAl4 Filler Metal. *Int. J. Adv. Manuf. Technol.* **2019**, *103*, 2485–2494. [CrossRef]
6. Satyanarayana, G.; Narayana, K.L.; Rao, B.N. Incorporation of Taguchi Approach with CFD Simulations on Laser Welding of Spacer Grid Fuel Rod Assembly. *Mater. Sci. Eng. B* **2021**, *269*, 115182. [CrossRef]
7. Paes, L.E.d.S.; Pereira, M.; de Souza Pinto Pereira, A.; Enrique Niño Borhóquez, C.; Lindolfo Weingaertner, W. Power and Welding Speed Influence on Bead Quality for Overlapped Joint Laser Welding. *J. Laser Appl.* **2019**, *31*, 022403. [CrossRef]
8. Wen-Hua, D.; Yun-Tao, S.; Ji-Jun, X.; Chao, F.; Jing, W.; Jie-Feng, W. Investigation on the Microstructure and Mechanical Properties of Autogenous Laser Welding Joint of ITER BTCC Case Lid. *Fusion Eng. Des.* **2020**, *156*, 111607.
9. Meng, X.; Bachmann, M.; Artinov, A.; Rethmeier, M. Experimental and Numerical Assessment of Weld Pool Behavior and Final Microstructure in Wire Feed Laser Beam Welding with Electromagnetic Stirring. *J. Manuf. Process.* **2019**, *45*, 408–418. [CrossRef]
10. Yan, S.; Meng, Z.; Chen, B.; Tan, C.; Song, X.; Wang, G. Prediction of Temperature Field and Residual Stress of Oscillation Laser Welding of 316LN Stainless Steel. *Opt. Laser Technol.* **2022**, *145*, 107493. [CrossRef]
11. Nabavi, S.F.; Farshidianfar, M.H.; Farshidianfar, A.; Beidokhti, B. Physical-Based Methodology for Prediction of Weld Bead Characteristics in the Laser Edge Welding Process. *Optik* **2021**, *241*, 166917. [CrossRef]
12. Kubiak, M.; Piekarska, W.; Stano, S.; Saternus, Z. Numerical Modelling of Thermal and Structural Phenomena in Yb:YAG Laser Butt-Welded Steel Elements. *Arch. Metall. Mater.* **2015**, *60*, 821–828. [CrossRef]
13. Zhang, S.; Kong, M.; Miao, H.; Memon, S.; Zhang, Y.; Liu, S. Transient Temperature and Stress Fields on Bonding Small Glass Pieces to Solder Glass by Laser Welding: Numerical Modelling and Experimental Validation. *Solar Energy* **2020**, *209*, 350–362. [CrossRef]
14. Filliard, G.; El Mansori, M.; De Metz-Noblat, M.; Bremont, C.; Reullier, A.; Tirado, L. Influence of Process Parameters on Thermal Cycle and Intermetallic Compounds Formation in High Speed Laser Weld-Brazing of Aluminium-Steel Angle Joints. *Procedia Manuf.* **2018**, *26*, 690–699. [CrossRef]
15. Kubiak, M.; Piekarska, W.; Stano, S. Modelling of Laser Beam Heat Source Based on Experimental Research of Yb:YAG Laser Power Distribution. *Int. J. Heat Mass Transf.* **2015**, *83*, 679–689. [CrossRef]
16. Rai, R.; Roy, G.G.; Debroy, T. A Computationally Efficient Model of Convective Heat Transfer and Solidification Characteristics during Keyhole Mode Laser Welding. *J. Appl. Phys.* **2007**, *101*, 054909. [CrossRef]
17. dos Santos Magalhães, E.; dos Santos Paes, L.E.; Pereira, M.; da Silveira, C.A.; de Souza Pinto Pereira, A.; Metrevelle Marcondes de Lima e Silva, S. A Thermal Analysis in Laser Welding Using Inverse Problems. *Int. Commun. Heat Mass Transf.* **2018**, *92*, 112–119. [CrossRef]
18. Rajesh, N.; Hynes, J.; Raja, S.; Angela, J.; Sujana, J.; Benita, B.; Sankaranarayanan, R. Numerical Simulation of Axial Shortening Distance in Friction Stud Welding of Aluminium/Mild Steel Joints. *Mater. Today Proc.* **2021**, *47*, 7127–7132. [CrossRef]
19. Paes, L.E.d.S.; da Silveira, C.A.; Pereira, M.; dos Santos Magalhães, E.; Vilarinho, L.O. Thermocouple Positioning through Capacitive Discharge for Temperature Monitoring in Laser Welding. *J. Braz. Soc. Mech. Sci. Eng.* **2021**, *43*, 468. [CrossRef]
20. Ahn, J.; He, E.; Chen, L.; Pirling, T.; Dear, J.P.; Davies, C.M. Determination of Residual Stresses in Fibre Laser Welded AA2024-T3 T-Joints by Numerical Simulation and Neutron Diffraction. *Mater. Sci. Eng. A* **2018**, *712*, 685–703. [CrossRef]
21. Duggirala, A.; Kalvettukaran, P.; Acherjee, B.; Mitra, S. Numerical Simulation of the Temperature Field, Weld Profile, and Weld Pool Dynamics in Laser Welding of Aluminium Alloy. *Optik* **2021**, *247*, 167990. [CrossRef]
22. Nayak, L.J.; Roy, G.G. Thermocouple Temperature Measurement during High Speed Electron Beam Welding of SS 304. *Optik* **2020**, *201*, 163538. [CrossRef]
23. Magalhaes, E.D.S.; Lima e Silva, A.L.F.d.; Lima e Silva, S.M.M. A GTA Welding Cooling Rate Analysis on Stainless Steel and Aluminum Using Inverse Problems. *Appl. Sci.* **2017**, *7*, 122. [CrossRef]
24. Yu, H.; Zhan, X.; Kang, Y.; Xia, P.; Feng, X. Numerical Simulation Optimization for Laser Welding Parameter of 5A90 Al-Li Alloy and Its Experiment Verification. *J. Adhes. Sci. Technol.* **2019**, *33*, 137–155. [CrossRef]

25. Ai, Y.; Jiang, P.; Shao, X.; Li, P.; Wang, C.; Mi, G.; Geng, S.; Liu, Y.; Liu, W. The Prediction of the Whole Weld in Fiber Laser Keyhole Welding Based on Numerical Simulation. *Appl. Therm. Eng.* **2017**, *113*, 980–993. [CrossRef]

26. Arunkumar, S.P.; Prabha, C.; Rajasekaran, S.; Khamaj, J.A.; Viswanath, M.; Ivan, C.K.P.; Subbiah, R.; Kumar, P.M. Taguchi Optimization of Metal Inert Gas (MIG) Welding Parameters to Withstand High Impact Load for Dissimilar Weld Joints. *Mater. Today Proc.* **2021**, *56*, 1411–1417. [CrossRef]

27. Yang, D.; Li, X.; He, D.; Nie, Z.; Huang, H. Optimization of Weld Bead Geometry in Laser Welding with Filler Wire Process Using Taguchi's Approach. *Opt. Laser Technol.* **2012**, *44*, 2020–2025. [CrossRef]

28. Narayana Reddy, B.; Hema, P.; Vishnu Vardhan, G.; Padmanabhan, G. Experimental Study of Laser Beam Welding Process Parameters on AISI 4130-309 Joint Strength. *Mater. Today Proc.* **2019**, *22*, 2741–2750. [CrossRef]

29. Magalhães, E.d.S.; Rodrigues de Carvalho, S.; Metrevelle Marcondes de Lima e Silva, S. The Use of Non-Linear Inverse Problem and Enthalpy Method in GTAW Process of Aluminum. *Int. Commun. Heat Mass Transf.* **2015**, *66*, 114–121. [CrossRef]

30. Li, B.Q. Free and Moving Boundary Problems. In *Discontinuous Finite Elements in Fluid Dynamics and Heat Transfer*; Springer: Berlin/Heidelberg, Germany, 2006; pp. 429–500. [CrossRef]

31. Incropera, F.P.; Dewitt, D.P.; Bergman, T.L.; Lavine, A.S. *Fundamentos de Transferência de Calor e Massa*, 6th ed.; LTC: New York, NY, USA, 2008.

32. Magalhães, E.d.S. A Quadrilateral Optimization Method for Nonlinear Thermal Properties Determination in Materials at High Temperatures. *Int. J. Heat Mass Transf.* **2021**, *181*, 121857. [CrossRef]

33. Borrmann, S.; Kratzsch, C.; Halbauer, L.; Buchwalder, A.; Biermann, H.; Saenko, I.; Chattopadhyay, K.; Schwarze, R. Electron Beam Welding of CrMnNi-Steels: CFD-Modeling with Temperature Sensitive Thermophysical Properties. *Int. J. Heat Mass Transf.* **2019**, *139*, 442–455. [CrossRef]

34. Clain, F.M.; Teixeira, P.R.d.F.; Araújo, d.D.B. Two Heat Source Models to Simulate Welding Processes with Magnetic Deflection. *Soldag. E Insp.* **2017**, *22*, 99–113. [CrossRef]

35. dos Santos Magalhães, E.; Fernandes de Lima e Silva, A.L.; Metrevelle Marcondes de Lima e Silva, S. A Thermal Efficiency Analysis of a Gas Tungsten Arch Welding Process Using a Temperature Moving Sensor. *Int. J. Therm. Sci.* **2018**, *129*, 47–55. [CrossRef]

36. Tadamalle, A.P.; Reddy, Y.P.; Ramjee, E.; Reddy, V. Evaluation of Nd: YAG Laser Welding Efficiencies for 304L Stainless Steel. *Procedia Mater. Sci.* **2014**, *6*, 1731–1739. [CrossRef]

37. Fakir, R.; Barka, N.; Brousseau, J.; Caron-Guillemette, G. Analysis of the Mechanical Behavior of AISI 4340 Steel Cylindrical Specimens Heat Treated with Fiber Laser. *J. Manuf. Process* **2020**, *55*, 41–56. [CrossRef]

38. Dourado da Silva, R.G.; dos Santos Magalhães, E.; Metrevelle Marcondes de Lima e Silva, S.; dos Santos Paes, L.E.; Pereira, M. Estimating the Absorption Efficiency in a Laser Welding Process Using a Nonlinear Inverse Problem Method. *Int. J. Therm. Sci.* **2023**, *183*, 107846. [CrossRef]

39. Montgomery, D.C. *Design and Analysis of Experiments*, 8th ed.; John Wiley & Sons, Inc.: Hoboken, NJ, USA, 1978; Volume 29, ISBN 9781118146927.

40. Devore, J.L. *Probability and Statistics for Engineering and Science*, 9th ed.; Cengage Learning: Boston, MA, USA, 2016; ISBN 978-0-538-73352-6.